AGU PUBLICATIONS

JGR

Journal of Geophysical Research: Oceans

RESEARCH ARTICLE

10.1002/2015JC011318

A wind-driven, hybrid latent and sensible heat coastal polynya off Barrow, Alaska

Daisuke Hirano[1], Yasushi Fukamachi[2], Eiji Watanabe[3], Kay I. Ohshima[2], Katsushi Iwamoto[1,4,5], Andrew R. Mahoney[6], Hajo Eicken[7], Daisuke Simizu[1], and Takeshi Tamura[1,8,9]

[1]National Institute of Polar Research, Tachikawa, Japan, [2]Institute of Low Temperature Science, Hokkaido University, Sapporo, Japan, [3]Japan Agency for Marine-Earth Science and Technology, Yokosuka, Japan, [4]Faculty of Science, Niigata University, Niigata, Japan, [5]Now at Mombetsu City, Mombetsu, Japan, [6]Geophysical Institute, University of Alaska Fairbanks, Fairbanks, Alaska, USA, [7]International Arctic Research Center, University of Alaska Fairbanks, Fairbanks, Alaska, USA, [8]The Graduate University for Advanced Studies, Tachikawa, Tokyo, Japan, [9]Antarctic Climate and Ecosystems Cooperative Research Centre, University of Tasmania, Hobart, Tasmania, Australia

Key Points:
- Nature of the Barrow Coastal Polynya (BCP) formed off the Alaska coast in winter is examined
- Ocean heat flux from upwelled warm water played an important role in formation of open water area
- BCP is a hybrid latent and sensible heat polynya, with both features caused by northeasterly wind

Correspondence to:
D. Hirano,
hirano.daisuke@nipr.ac.jp

Citation:
Hirano, D., Y. Fukamachi, E. Watanabe, K. I. Ohshima, K. Iwamoto, A. R. Mahoney, H. Eicken, D. Simizu, and T. Tamura (2016), A wind-driven, hybrid latent and sensible heat coastal polynya off Barrow, Alaska, *J. Geophys. Res. Oceans*, *121*, 980–997, doi:10.1002/2015JC011318.

Received 13 SEP 2015
Accepted 3 JAN 2016
Accepted article online 8 JAN 2016
Published online 29 JAN 2016

Abstract The nature of the Barrow Coastal Polynya (BCP), which forms episodically off the Alaska coast in winter, is examined using mooring data, atmospheric reanalysis data, and satellite-derived sea-ice concentration and production data. We focus on oceanographic conditions such as water mass distribution and ocean current structure beneath the BCP. Two moorings were deployed off Barrow, Alaska in the northeastern Chukchi Sea from August 2009 to July 2010. For sea-ice season from December to May, a characteristic sequence of five events associated with the BCP has been identified; (1) dominant northeasterly wind parallel to the Barrow Canyon, with an offshore component off Barrow, (2) high sea-ice production, (3) upwelling of warm and saline Atlantic Water beneath the BCP, (4) strong up-canyon shear flow associated with displaced density surfaces due to the upwelling, and (5) sudden suppression of ice growth. A baroclinic current structure, established after the upwelling, caused enhanced vertical shear and corresponding vertical mixing. The mixing event and open water formation occurred simultaneously, once sea-ice production had stopped. Thus, mixing events accompanied by ocean heat flux from the upwelled warm water into the surface layer played an important role in formation/maintenance of the open water area (i.e., sensible heat polynya). The transition from a latent to a sensible heat polynya is well reproduced by a high-resolution pan-Arctic ice-ocean model. We propose that the BCP, previously considered to be a latent heat polynya, is a wind-driven hybrid latent and sensible heat polynya, with both features caused by the same northeasterly wind.

1. Introduction

Polynyas are persistent and recurrent areas of open water and/or thin ice, where heat loss to the atmosphere is one or two orders of magnitude larger than over thick ice [*Maykut*, 1978]. Polynyas can be classified into two types: latent heat and sensible heat polynyas. The former is the result of divergent ice motion due to prevailing winds and/or ocean currents, whereas the latter is due to high surface ocean heat fluxes [*Morales Maqueda et al*., 2004]. Whereas most Arctic polynyas are thought to be latent heat polynyas, the ocean heat flux from the underlying warm water partly contributes to the presence of the North Water (NOW) polynya in Baffin Bay near Greenland [*Ingram et al*., 2002]. Note that high ice production in the NOW polynya occurs due to the ice bridge in the southern Nares Strait that prevents ice drift from the Arctic Ocean to Baffin Bay [*Mundy and Barber*, 2001], prevailing southward winds [*Barber et al*., 2001], and southward water flow from the Arctic Ocean [*Melling et al*., 2001]. In the case of Arctic coastal polynyas over a shallow continental shelf, the underlying ocean heat content is generally expected to be small since the whole water column likely reaches the freezing point in winter [*Winsor and Björk*, 2000]. Therefore, most heat loss in Arctic coastal polynyas over the shallow continental shelf is balanced by sea ice production, which results in dense water formation due to brine rejection. Assuming that all heat loss is balanced by ice production, the ice production rate over the thin ice areas can be estimated from heat budget analyses [e.g., *Cavalieri and Martin*, 1994; *Martin et al*., 2004; *Tamura and Ohshima*, 2011; *Iwamoto et al*., 2014]. By contrast, over sensible heat polynyas, the assumption of negligible upward ocean heat flux would result in the overestimation of ice production because most of the surface heat lost to the atmosphere goes into cooling

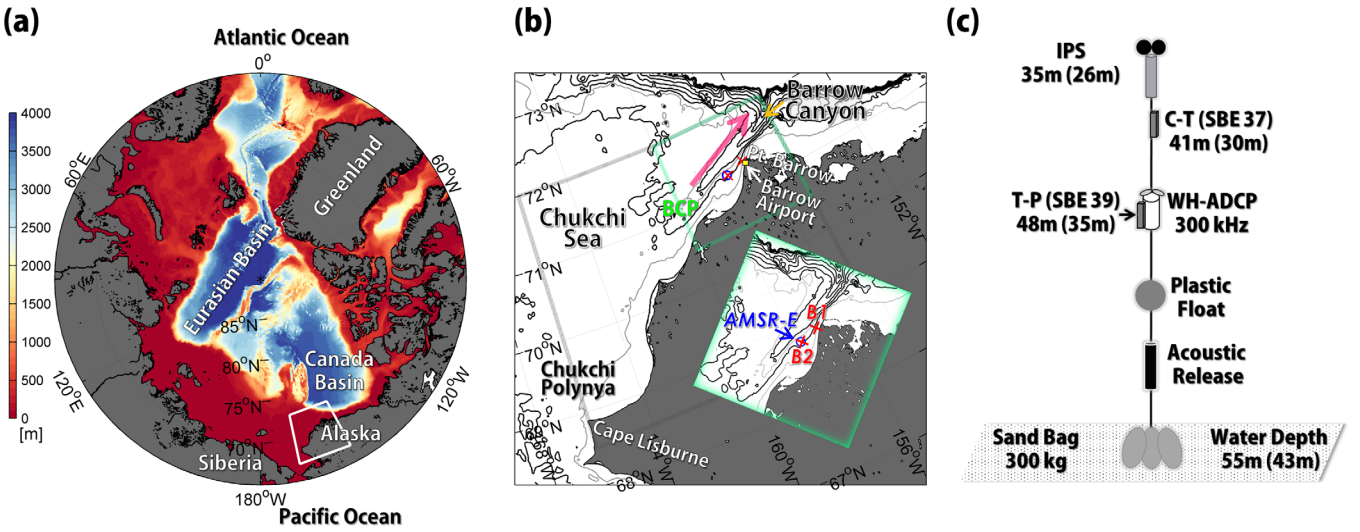

Figure 1. (a) Bathymetry of the Arctic Ocean from the International Bathymetric Chart of the Arctic Ocean (IBCAO version 3.0). The enclosed region is shown in Figure 1b. (b) Bathymetry around the mooring sites on the northeastern Chukchi shelf. The gray and green-enclosed regions represent the Chukchi Polynya and Barrow Coastal Polynya (BCP), respectively. Inset at the bottom right is the region around the mooring sites in the BCP. Red crosses represent moorings B1 (71.33°N, 156.89°W, water depth of 43 m) and B2 (71.23°N, 157.65°W, water depth of 55 m). Blue circle represents the location of the nearest AMSR-E grid point to B2 (71.25°N, 157.69°W). Yellow square near Pt. Barrow indicates the location of Barrow Wiley-Post Airport. Direction of along-Barrow Canyon (63°T: 0°T corresponds to the north) is also indicated by the pink arrow. (c) Mooring configurations at B1 and B2. Nominal depths of instruments are indicated for B2 and B1 (in parentheses).

the underlying water column. Using the Special Sensor Microwave/Imager (SSM/I) data, *Tamura and Ohshima* [2011] provided the first mapping of ice production in the entire Arctic. Recently, *Iwamoto et al.* [2014] improved the mapping of ice production in the Arctic using the Advanced Microwave Scanning Radiometer-Earth Observing System (AMSR-E) with higher spatial resolution with various masks (detecting open water and landfast ice) to correct the overestimation in the previous mapping by *Tamura and Ohshima* [2011]. The Barrow Coastal Polynya (BCP, hereafter), a part of the Chukchi Polynya located between Cape Lisburne and Point Barrow along the Alaska coast (see Figure 1b for locations), is formed by predominantly offshore wind in winter [*Cavalieri and Martin*, 1994 among others]. The mean value of annual cumulative ice production in the Chukchi Polynya has been estimated as 2.2 ± 0.4 m for 2002/2003–2010/2011 [*Iwamoto et al.*, 2014].

Pacific-origin water entering the Chukchi Sea through the Bering Strait, with a mean annual transport of 0.8 Sv (1 Sv = 10^6 m^3 s^{-1}) [*Roach et al.*, 1995; *Woodgate et al.*, 2006], reaches the Chukchi Sea shelf break via three pathways; Barrow Canyon on the eastern Chukchi shelf [*Weingartner et al.*, 1998, 2005; *Pickart et al.*, 2005], the Central Channel between the Herald and Hanna Shoals [*Weingartner et al.*, 2005], and Herald Canyon on the western Chukchi shelf [*Woodgate et al.*, 2005]. In Barrow Canyon, persistent northward flow is intensified in summer and slows down in winter [*Aagaard and Roach*, 1990; *Weingartner et al.*, 1998, 2005; *Itoh et al.*, 2013]. Properties of the Pacific-origin water vary seasonally alternating between warm, relatively fresh Pacific Summer Water (PSW) and cold, relatively saline Pacific Winter Water (PWW). In winter, PWW is affected by atmospheric cooling and ice production in the Chukchi Sea. Therefore, properties of PWW around Barrow Canyon depend on the original salinity of Pacific-origin water at Bering Strait and the amount of additional salt input along the PWW pathway, flowing through the BCP toward Barrow Canyon [*Itoh et al.*, 2012]. Sinking of dense shelf water produced in the BCP maintains the cold halocline layer (or cold halostad layer, CHL) that thermally insulates the cold, fresh surface mixed layer from the deep warm, saline Atlantic Water [*Aagaard et al.*, 1981; *Rudels et al.*, 1996; *Winsor and Björk*, 2000; *Fer*, 2009]. In addition, the volumetric input of PWW into the Canada Basin affects the upper ocean circulation of the Beaufort Gyre, because the inflow of PWW forms a potential vorticity minimum layer [*Itoh et al.*, 2012].

Warm, saline Atlantic Water (AW) is centered on 300–400 m water depth throughout the southern Canada Basin [e.g., *Jackson et al.*, 2010] and below ~150 m in Barrow Canyon [*Itoh et al.*, 2013]. From late autumn to winter, strong northerly winds inhibit northward transport of the Pacific-origin water through Barrow Canyon, and bring warm AW into the canyon [*Aagaard and Roach*, 1990; *Woodgate et al.*, 2005]. Upwelled AW

has been also observed on the Beaufort shelf along the northern Alaska coast. This upwelling is caused by northeasterly winds associated with the Aleutian Low and the Beaufort High [*Pickart et al*., 2009]. While the BCP has been regarded as a latent heat polynya [*Winsor and Björk*, 2000; *Cavalieri and Martin*, 1994; *Martin et al*., 2004] where ice production is enhanced by winds and ocean currents, *Itoh et al*. [2012] have argued that the return flow of warm PSW from the basin reduced the amount of ice production in winter of 2003/2004. However, their argument is based on an ocean temperature time series obtained at the mouth of Barrow Canyon, not in the BCP. Based on time series by Ice-profiling sonars (IPS), *Ito et al*. [2015] detected signals of frazil ice formation accompanied by potentially supercooled water in the BCP. They reported that these signals vanished with the arrival of warm AW in the BCP. These recent studies therefore suggest that the BCP may have characteristics of a sensible heat polynya as well. However, details of the underlying processes, in particular how ocean heat flux due to the warm water inflow from the Canada Basin reduces the ice production in the BCP, have not been well described. In this study, we examine the nature of the BCP using data from year-long under-ice moorings, satellite-derived products (sea ice concentration and production rate), atmospheric reanalysis data, and tracer experiment results from a high-resolution pan-Arctic ice-ocean model. Specifically, we focus on oceanographic conditions such as water mass distribution and ocean current structure in the BCP, which have not been fully documented.

In the following, section 2 provides a brief overview of the mooring observations in the BCP, satellite-derived and atmospheric reanalysis data, and the pan-Arctic ice-ocean model. Section 3 presents the characteristics of the BCP events revealed mainly through mooring observations. Section 4 then provides our discussion on the transition process of BCP from a latent to a sensible heat polynya, based on the integrated analysis. Finally, section 5 provides concluding remarks.

2. Data and Methods

2.1. Mooring Observations in the BCP

Two moorings were deployed off Barrow, Alaska in the northeastern Chukchi Sea (B1 at 71.33°N, 156.88°W in a water depth of 43 m and B2 at 71.23°N, 157.65°W in a water depth of 55 m) from August 2009 to July 2010 (Figures 1a and 1b). The distance between B1 and B2 is ∼30 km. In winter, landfast ice often exists around B1 [*Petrich et al*., 2012; *Mahoney et al*., 2014, 2015] and a polynya forms around B2 [*Tamura and Ohshima*, 2011; *Iwamoto et al*., 2013, 2014]. A grid point of Advanced Microwave Scanning Radiometer-Earth Observing System (AMSR-E) is located close to B2 at 71.25°N, 157.69°W (Figure 1b). The two moorings are composed with the same configurations; an Ice Profiling Sonar (IPS; ASL Environmental Sciences IPS5) to measure ice thickness, an Acoustic Doppler Current Profiler (ADCP; Teledyne RD Instruments WH-Sentinel 300 kHz), a temperature-pressure recorder (Sea-Bird Electronics SBE39), and a temperature-conductivity recorder (Sea-Bird Electronics SBE37) (Figure 1c). Sampling intervals of the IPS, ADCP, and SBE37/39 are 1 s, 15 min, and 5 min, respectively. Ocean current data are resampled every hour. Note that ocean current data are flagged when the ADCPs tilted over 20°. The observational data used in this study are available from the ACADIS Gateway (https://www.aoncadis.org/dataset/mooring_temperatureconductivity__temperaturepressure_data.html; https://www.aoncadis.org/dataset/mooring_adcp_data.html) as part of the Seasonal Ice Zone Observing Network (SIZONet) [*Fukamachi et al*., 2014; *Eicken et al*., 2014].

2.2. Satellite and Meteorological Data

In this study, we use daily sea ice concentration (SIC) data from the Bootstrap Basic Algorithm (BBA) [*Comiso*, 1995] extracted from the AMSR-E/Aqua Level 3 product [*Cavalieri et al*., 2004]. AMSR-E-derived daily ice production data estimated from the heat budget analysis [*Iwamoto et al*., 2014] are also used, based on the linear relationship between ice production rate and heat loss at the ice surface. The heat budget analysis assumes that the sum of radiative and turbulent fluxes at the ice surface is balanced by the conductive heat flux in the ice, whose thickness is derived by the AMSR-E thin ice thickness algorithm [*Iwamoto et al*., 2013]. Using the empirical formula of each flux component, the ice surface temperature can be calculated to be balanced. Then, the conductive heat flux, corresponding to the heat loss, can be obtained. Finally, sea ice production is calculated assuming that all of the heat loss goes into ice formation. The thin ice algorithm provides estimates of ice thickness in the range of 0–0.2 m from the polarization ratio (PR) of the horizontally and vertically polarized AMSR-E brightness temperatures at 89 and 36 GHz using an empirically derived PR—thickness relationship. At present, this data set is of the highest spatial resolution with the open water

mask [*Iwamoto et al*., 2013] and landfast ice mask [*Iwamoto et al*., 2014]. The open water mask can identify open water areas (i.e., sensible heat polynyas) where the previous methods [*Tamura and Ohshima*, 2011] tend to yield false ice production. Spatial resolutions of AMSR-E-derived SIC and ice production data are 12.5 and 6.25 km, respectively. We use wind speed/direction observed hourly at Barrow Wiley-Post Airport (see Figure 1b for the location). We also use sea level pressure (SLP) and wind speed/direction at 10 m height (U10 and V10) provided by the European Centre for Medium-Range Weather Forecasts (ECMWF) Interim Re-Analysis (ERA-Interim).

2.3. Pan-Arctic Ice-Ocean Model

The model configuration and experimental design are the same as those in the previous seasonal experiments [*Watanabe et al*., 2014, 2015] except for the target period. The coupled sea ice-ocean model used in this study is Center for Climate System Research Ocean Component Model (COCO) version 4.9 [*Hasumi*, 2006]. The COCO model reasonably reproduces major features of ocean circulation in the Chukchi Sea [*Watanabe*, 2011]. The sea ice part includes a multi-thickness-category configuration based on that of *Bitz et al*. [2001] with one-layer thermodynamic formulation [*Bitz and Lipscomb*, 1999] and the elastic-viscous-plastic rheology [*Hunke and Dukowicz*, 1997]. The ocean component is a free-surface ocean general circulation model formulated with the advection scheme of *Leonard et al*. [1994], the Smagorinsky-type harmonic viscosity [*Griffies and Hallberg*, 2000], and the turbulence closure scheme of *Noh and Kim* [1999]. The horizontal diffusivity is set to 2.0 $m^2\ s^{-1}$. Vertical penetrative convection induced by unstable stratification is not explicitly represented by the COCO model, which employs the hydrostatic approximation and does not resolve the actual horizontal scale of convective plumes [*Hasumi*, 2006]. Instead, the classical convective adjustment scheme is adopted such that unstable density profiles are artificially homogenized with conserving heat and salt in a single model time step (i.e., 2 min in the present case). The model domain contains the entire Arctic Ocean, the Greenland-Iceland-Norwegian (GIN) seas, and the northern part of the North Atlantic [see *Watanabe et al*., 2015, Figure 1]. There are 42 hybrid σ-z vertical levels. The vertical grid spacing varies from 2 m at the top level to 500 m at the bottom level. For the tracer experiments described in section 4.2, we integrate the 5 km grid model from October 2009 to September 2010. The integration period is intended to cover winter polynya events. The initial sea ice and ocean fields for this seasonal experiment are obtained from the decadal experiment from 1979 to 2009 using the 25 km grid version [cf. *Watanabe*, 2013]. The atmospheric forcing components are constructed from the National Centers for Environmental Prediction-Climate Forecast System Reanalysis (NCEP-CFSR) 6 hourly data set [*Saha et al*., 2010]. In the Bering Strait, Pacific water inflow with a seasonal cycle is specified as in *Watanabe* [2011].

3. Results

3.1. Seasonal Variations in Water Mass Property

As mentioned in section 1, the BCP is located within the pathway of Pacific-origin water entering the Canada Basin via Barrow Canyon. In addition, the Chukchi shelf-Canada Basin interaction occasionally occurs through upwelling of warm AW around Barrow Canyon [*Aagaard and Roach*, 1990; *Woodgate et al*., 2005]. Therefore, various water masses are expected to be present on the shelf region around Barrow Canyon due to the seasonal variability of Pacific-origin water and/or the upwelling of AW. Figure 2 shows relationships of temperature (relative to freezing point T_f) and salinity at B2 (41 m) from August 2009 to July 2010. We use the water mass definitions by *Itoh et al*. [2013] as follows; PSW ($S < 32.5$ with $T > T_f + 1°C$), PWW ($32.5 < S < 34$—with some exceptions detailed below—with $T < T_f + 1°C$), and AW ($S > 34$ with $T > T_f + 1°C$). Warm and fresh PSW was observed from August to early November. PSW temperatures began to decrease through atmospheric cooling in October, and its water properties evolved into those of PWW near the freezing point after mid-November. Although some PWW from November to June was clearly fresher than its defined lower salinity limit of $S = 32.5$, we still classify a water mass with $T < T_f + 1°C$ as PWW because PSW generally has not been found during the ice-growth season. Except for the upwelling events of warm water described below, the observed temperature and salinity of PWW were near the freezing point and ~32, respectively. The water temperature increased after June, PSW was then dominant in this region. AW signals were frequently found from October to early June as shown in shifts toward the upper right in Figure 2, although they were less clear in April. Except for summer and early fall when PSW was dominant, these AW signals resulted from the upwelling caused by northeasterlies blowing in the direction of Barrow Canyon (see section 3.3).

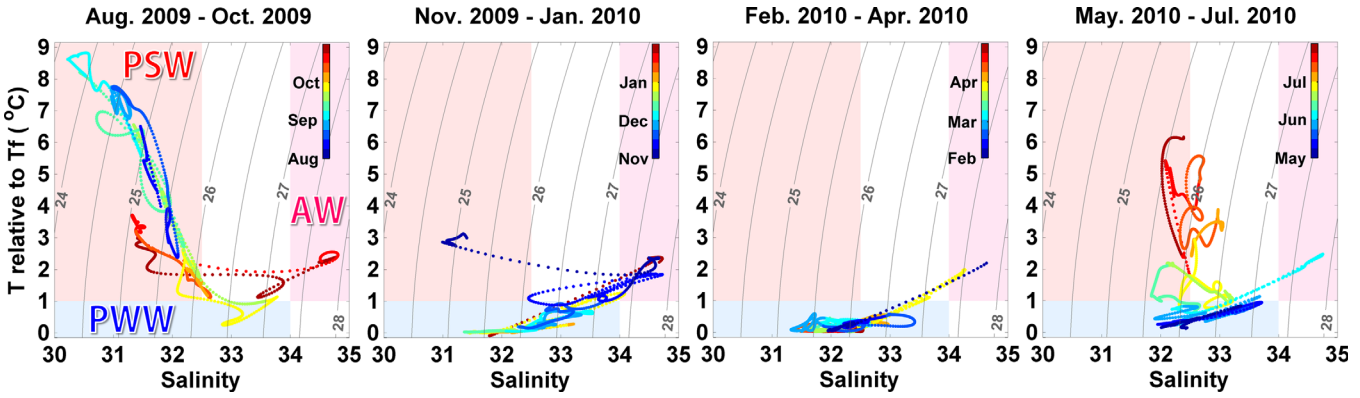

Figure 2. Relationship between temperature (relative to freezing point) and salinity at 41 m of B2 from August 2009 to July 2010 after applying a tide killer filter [*Thompson*, 1983]. Colors of dots indicate time in each month. Red, light blue, and pink-shaded areas represent water mass classifications for Pacific Summer Water (PSW; $T > T_f + 1$°C with $S < 32.5$), Pacific Winter Water (PWW; $T < T_f + 1$°C with $S < 34$), and Atlantic Water (AW; $T > T_f + 1$°C with $S > 34$) [after *Itoh et al.*, 2013]. The gray contours denote potential density surfaces.

3.2. BCP Events

Time series of wind, SIC, and ice production from November to May are shown in Figures 3a and 3b. The SIC started increasing in mid-November and decreasing in late April, and then dropped to zero in June. Considering this seasonal variability, the ice-growth period around Barrow Canyon in 2009/2010 is defined to be from mid-November to mid-May. During this period, the region around Barrow Canyon was almost entirely covered by sea ice (i.e., SIC is 100%) except for BCP events defined below. We identified five BCP events (highlighted in Figure 3) and refer to each BCP event as Events 1–5. Table 1 summarizes characteristics of these events. Minimum and maximum durations of the BCP events were 4 days in Event 2 and 17 days in Event 4, respectively. The area of the BCP differed between events (Figure 4). The dominant winds during the BCP events were commonly northeasterly (toward 240°T on average (from 60°T): 0°T corresponds to the north) (Figures 3, 4, and Table 1). These northeasterly winds resulted from a pressure pattern dominated by the Aleutian Low and Beaufort High (Figures 4a and 4b). Their direction was almost parallel to the Barrow Canyon with an offshore component near Barrow. Previous studies reported a similar relationship between formation of the Chukchi Polynya and dominant offshore winds [e.g., *Tamura and Ohshima*, 2011; *Kawaguchi et al.*, 2011]. For each BCP event, active ice production occurred with rates of 0.05–0.10 m d^{-1} and the maximum exceeding ~0.15 m d^{-1} (Figure 3b, green bars). For a latent heat polynya, ice growth is expected to be continuous while the polynya remains open. However, in each BCP event, ice production was not quite continuous and suddenly dropped to zero in most BCP events (Figure 3b, green bars) if the open water mask of AMSR-E is assumed to be correct. This is a remarkable feature of the BCP events. A possible process leading to the suppression of sea ice growth during the BCP events will be discussed in detail in section 4.1.

3.3. Upwelled Warm Water Beneath the BCP

Figures 3c and 3d show time series of temperature (relative to the freezing point), salinity, and potential density obtained at B2 (41 m). During the BCP events, warm and saline (dense) AW appeared at the moorings, with the most prominent signals of $T > T_f + 2$°C, $S > 34$, and $\sigma_\theta > 27$ kg m^{-3} (Figures 2, 3c, and 3d). Whenever the BCP was open, these signals appeared and peaked after the onset of SIC decrease. Throughout the ice-growth period, it is reasonable to consider that temperature is vertically uniform and near the freezing point over the shallow shelf (Figures 3c and 5b). In contrast, the upwelled warm water is considered to be present below the surface mixed layer, resulting in two-layer thermal structure.

Dominant northeasterly winds over the BCP region induce two different phenomena as follows: (1) sea ice divergence causing the formation of the BCP and (2) upwelling of warm and saline water, originating from the mouth of Barrow Canyon and the southern Canada Basin, compensating surface Ekman flow toward the offshore. Thus, the combination of the coastline orientation around Barrow and the location of Barrow Canyon along with prevailing northeasterly winds can result in both enhancement and inhibition of ice production in the BCP. Unless the upwelled warm water outcrops, upward heat transport accompanied by vertical mixing into the surface mixed layer is required to suppress ice production and/or to melt sea ice. Such

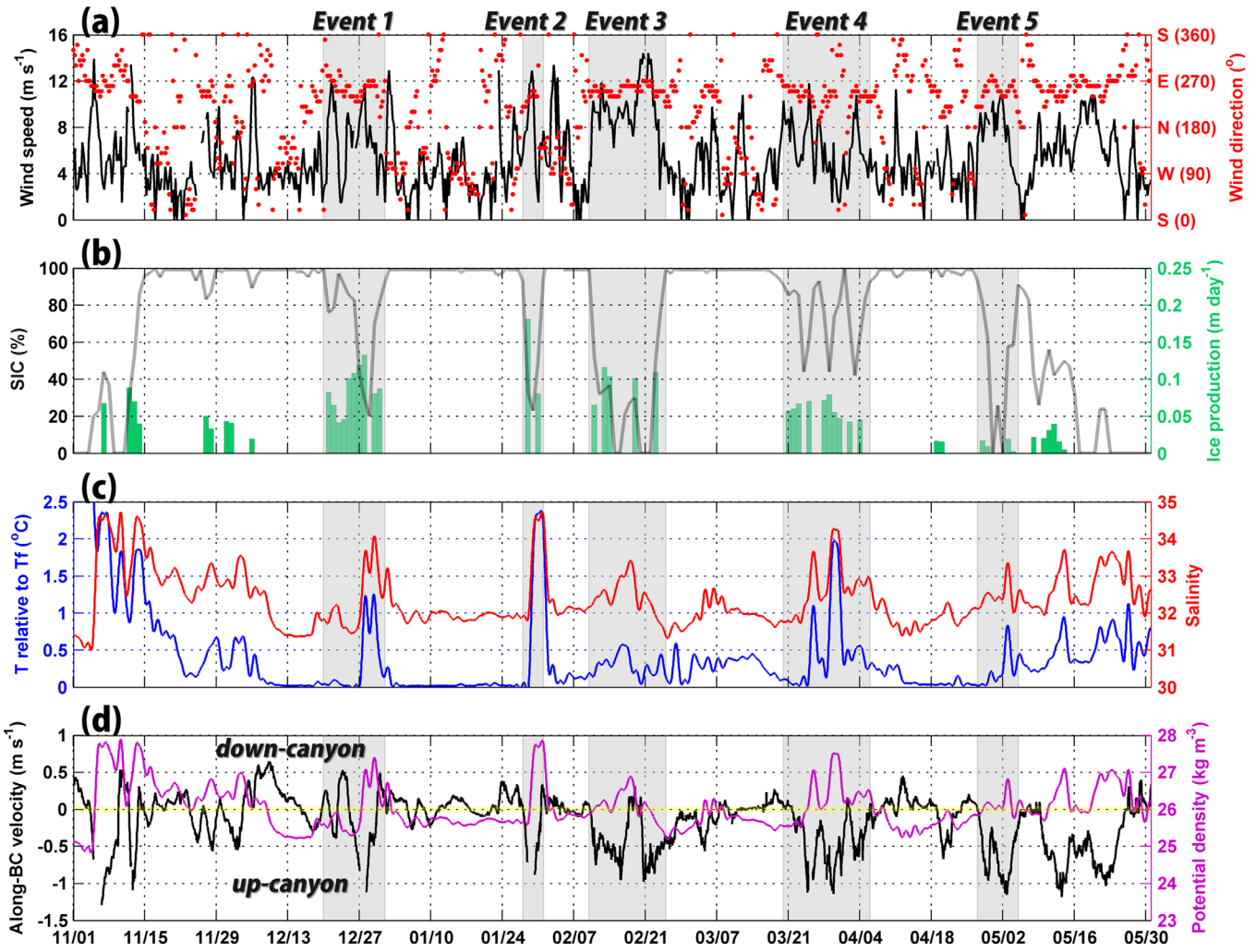

Figure 3. Time series of (a) wind speed (solid line) and direction (red dots) at Barrow Wiley-Post Airport, (b) sea ice concentration (solid line), and production rate (green bar) at the AMSR-E grid point shown in Figure 1b, (c) temperature relative to freezing point (blue), and salinity (red) at 41 m after applying a tide killer filter [*Thompson*, 1983], (d) along-BC velocity at 11 m (black, positive values indicate down-canyon flows) and potential density at 41 m (purple). Blanks in Figure 3d represent the flagged data (see section 2.1). Shadings represent periods of BCP events. Data at B2 are shown in Figures 3c–3d.

upward heat transport transforms the BCP into a sensible heat polynya in which heat loss mostly goes into cooling of the water column and/or suppression of ice growth. Our mooring observations clearly revealed that the seawater beneath the BCP is not necessarily at the freezing point throughout the whole water column. For this reason, the assumption of negligible ocean heat flux results in a significant bias in the satellite-based estimates of ice production for the BCP.

Figures 5b and 6b show time series of the temperature at B1 and B2 for Events 1 and 3. Temperature data recorded by the topmost IPSs indicate that the upwelled warm water reached at least 26 and 35 m below the surface at B1 and B2, respectively. The temperature was higher at deeper sensors during upwelling episodes. In addition, warm signals appeared first at B1 and were stronger than those at B2. This suggests that the upwelled warm water was modified by mixing processes during its transport from Barrow Canyon to the mooring region.

3.4. Up-Canyon Shear Flow Due to Upwelling

Figure 3d shows a time series of ocean current along the Barrow Canyon (63°T; along-BC velocity, hereafter) at B2 (11 m). Down-canyon flow toward the Canada Basin was up to ~0.5 m s^{-1}. However, each time the BCP started forming, up-canyon flow toward the BCP region gradually strengthened and reached its maximum of up to ~1 m s^{-1} nearly coincident with the local SIC minimum (Figure 3b). In addition, the up-

Table 1. Characteristics of BCP Events 1–5[a]

Polynya Event	Date	Duration (days)	Wind Direction (°T)	Wind Speed (m s^{-1})	Air Temp. (°C)	SIC (%)	Ice Production Rate (m d^{-1})	Along-BC Velocity at 11 m (63°T, m s^{-1})	Temp. at 35 m (°C)	Temp. at 41 m (°C)	Temp. at 48 m (°C)	Sal. at 41 m	σ_θ at 41 m (kg m^{-3})
Freeze-up period	15 Nov 2009 to 15 May 2010	181	206	5.3	−20.1	83.0	0.015	−0.13	−1.61	−1.51	−1.47	32.29	25.97
	Except Polynya Events	124	189	4.4	−20.9	94.9	0.003	−0.03	−1.64	−1.57	−1.54	32.16	25.87
Event 1	20 Dec 2009 to 1 Jan 2010	12	250	6.7	−19.8	72.8	0.067	−0.07	−1.61	−1.49	−1.43	32.32	26.00
Event 2	28 Jan 2010 to 1 Feb 2010	4	216	7.7	−22.1	58.4	0.052	−0.30	−0.67	−0.57	−0.57	33.41	26.84
Event 3	10 Feb 2010 to 25 Feb 2010	15	252	9.3	−19.2	35.0	0.031	−0.43	−1.62	−1.51	−1.43	32.45	26.10
Event 4	20 Mar 2010 to 6 Apr 2010	17	238	6.0	−19.4	75.7	0.033	−0.38	−1.48	−1.31	−1.18	32.70	26.30
Event 5	27 Apr 2010 to 5 May 2010	9	249	7.5	−8.5	52.1	0.006	−0.63	−1.69	−1.58	−1.54	32.47	26.12
	Average for Polynya Events	11	241	7.4	−17.8	58.8	0.038	−0.36	−1.41	−1.29	−1.23	32.67	26.27

[a]Durations, wind speed/direction, air temperature (at Barrow Wiley-Post Airport), sea ice concentration, ice production rate (at the AMSR-E grid point nearest to B2), along-BC velocity (63°T), temperature, salinity, and potential density at B2.

canyon flow corresponded with higher potential density, likely caused by the upward displacement of density surfaces due to the upwelling.

Before the upwelling, the along-BC velocity was nearly uniform vertically (Figures 5c and 6c), and thereby vertical shear was small except near sea surface (Figures 5d and 6d). After the upwelling, the velocity structure became baroclinic, and thereby the vertical shear was enhanced. During Event 1 (29–30 December), directions of ocean currents in the upper and lower layers were out of phase with each other, resulting in the enhanced vertical shear in the whole water column. It is likely that in particular the enhanced vertical shear in the lower layer contributed to the upward heat transport because the upwelled warm water reached to at least ∼30 m depth immediately below the surface mixed layer. Further, high-frequency variability in subsurface temperature during the enhanced vertical shear is additional evidence of possible vertical mixing there. Even though wind conditions exhibited little variability during the BCP event, the vertical shear structure was dramatically altered due to the upwelling, and in some cases the vertical shear was locally enhanced in the lower layer (Figures 5 and 6). In the northern Chukchi shelf in summer, *Rainville and Woodgate* [2009] argued that a near-inertial internal wave induced by wind stress contributed to the vertical mixing in an open water area. In the BCP in winter, however, vertical mixing is considered to be enhanced by the baroclinic current structure established after the wind-driven upwelling, rather than wind stress directly stirring the water column. Along with the current shear, mixing can be enhanced by vertical convection driven by surface cooling and/or brine rejection (see section 4.2).

4. Discussion

4.1. Transition Process From Latent to Sensible Heat Polynya off Barrow

As mentioned in section 3.3, the dominant northeasterly winds can result in both the enhancement and inhibition of ice production in the BCP. From our mooring observations, however, it is not possible to deduce whether the upwelled warm water actually reached the sea surface. Therefore, the linkage between ocean heat transport caused by the upwelling and suppression of the ice production in the BCP cannot be explained, unless the vertical mixing plays a key role in resultant upward heat flux from the upwelled warm water. If temperature in the surface mixed layer rises above the freezing point as a result of the upward heat flux, heat loss to the atmosphere mostly goes into cooling the surface mixed layer rather than producing sea ice. The result is that the BCP possibly changes from a latent to a sensible heat polynya. In fact, open water area (Figure 7, orange dots) is formed/maintained when the vertical shear is enhanced especially in the lower layer after the upwelling (Figures 5 and 6). This strongly indicates that the open water area (i.e., sensible heat polynya) is caused by the influence of ocean heat transport from the upwelled warm water through vertical mixing.

It is difficult for any mooring in ice-covered regions to measure water properties near the surface due to the risk of collision with thick ridged ice. Thus, we indirectly estimate the ocean heat flux and its influence on the ice production, not based on variability of stratification and temperature in the surface mixed layer. If we assume that only the ocean heat transport maintains the sensible heat polynya over several days, we can conservatively estimate the lower limit of the ocean heat flux. To take Event 3 in February 2010 as an

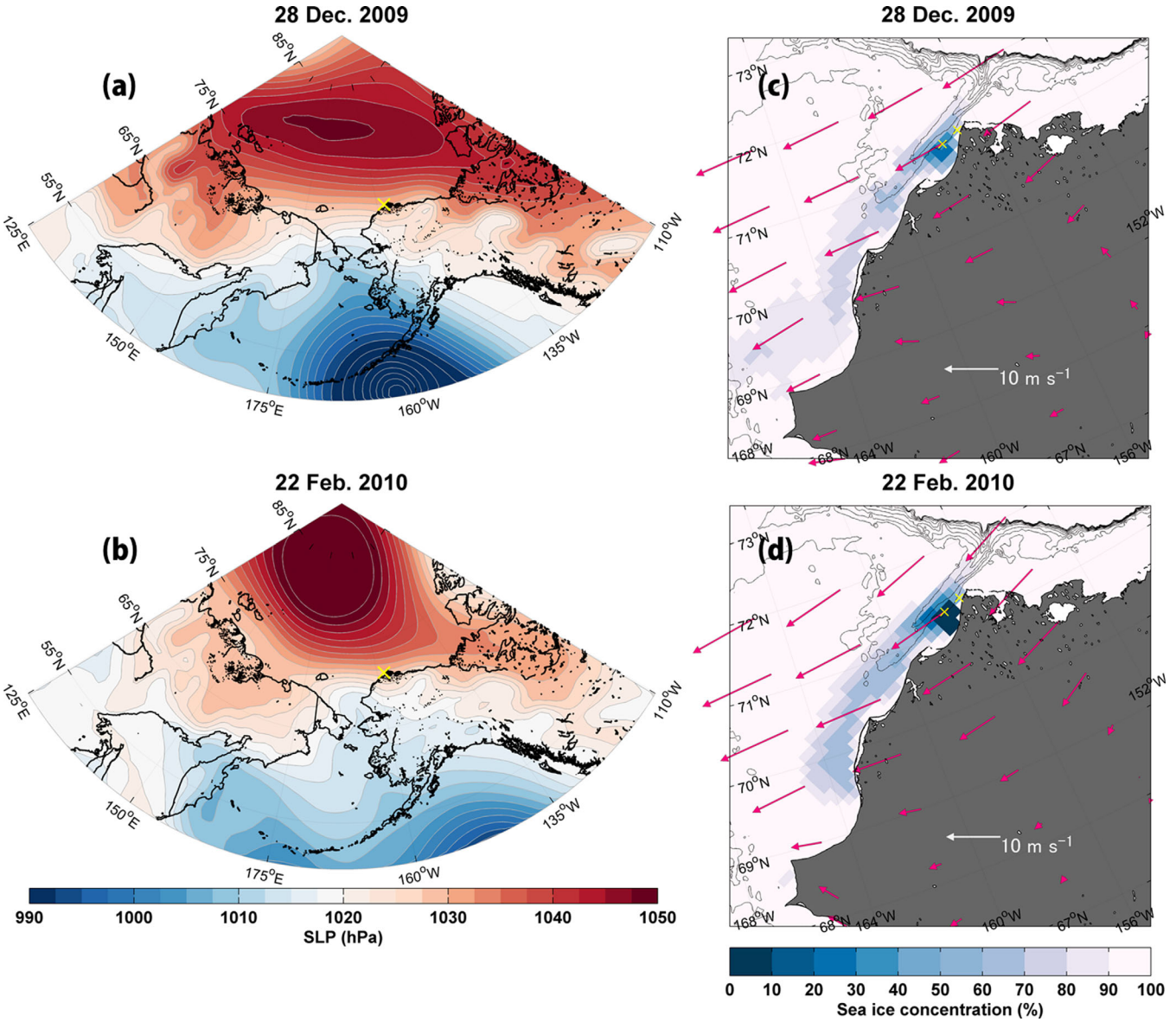

Figure 4. Spatial distributions of (a, b) sea level pressure (SLP) and (c, d) sea ice concentration (shade) and 10 m wind (vector) on 28 December 2009 (Event 1) and 22 February 2010 (Event 3). The SLP and 10 m wind data are from ERA-interim.

example, averaged heat losses to the atmosphere, $Q_{loss,}$ for open water periods A (15–18 February) and B (20–22 February) judged by the open water mask (Figure 8a) are estimated to be 461 and 591 W m^{-2}, respectively. It is normally expected that the open water area freezes immediately due to these large values of Q_{loss} and is covered by newly-formed thin ice. Actually, however, ice production was suppressed as the open water area was maintained. This indicates that the ocean heat flux, Q_{ocean}, is equal to or larger than Q_{loss}. These large values of Q_{ocean} require energetic vertical mixing, as suggested by the enhanced vertical shear (Figures 5d and 6d). For simplicity, the water column is assumed to consist of two layers: the surface mixed layer at the freezing point and the upwelled warm water below (see section 3.3), and central depths of the upper and lower layers are set to be 15 and 40 m, respectively. The vertical ocean heat flux due to turbulence is given by $Q_{ocean}=\rho C_p K_T d_T/d_z$. Here, ρ is sea water density (kg m^{-3}), C_p is the specific heat (J $kg^{-1}°C^{-1}$), K_T is the heat diffusivity (m^2 s^{-1}), d_T is difference of temperature between upper and lower layers (°C), and d_Z is vertical distance between central depths of upper and lower layers (m). In the present case, d_Z is 25 m and d_T corresponds to the deviation from the freezing point as shown in Figure 8a. Using these

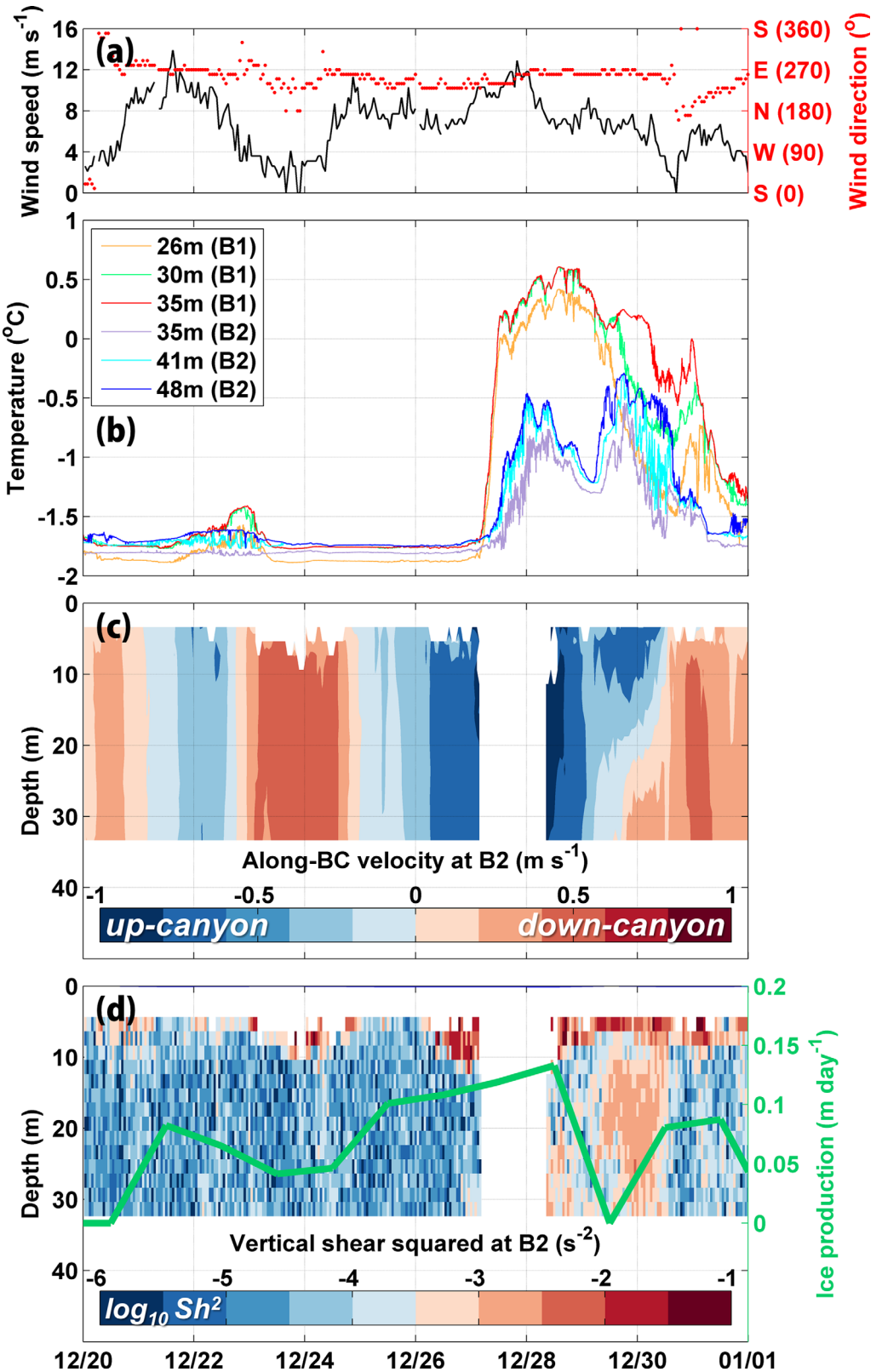

Figure 5. Time series of (a) wind speed (black) and direction (red dots) at Barrow Wiley-Post Airport, (b) temperature at B1 (orange: 26 m, green: 30 m, red: 35 m) and B2 (light purple: 35 m, light blue: 41 m, blue: 48 m), vertical sections of (c) along-BC velocity (positive values indicate down-canyon flows) and (e) logarithmic vertical shear squared (shade) at B2 and daily ice production rate at the AMSR-E grid point shown in Figure 1b (green) during BCP Event 1. Note that the temperatures shown in Figure 5b are raw data, unlike in Figures 2 and 3c. Blanks in Figures 5c and 5d represent the flagged data (see section 2.1).

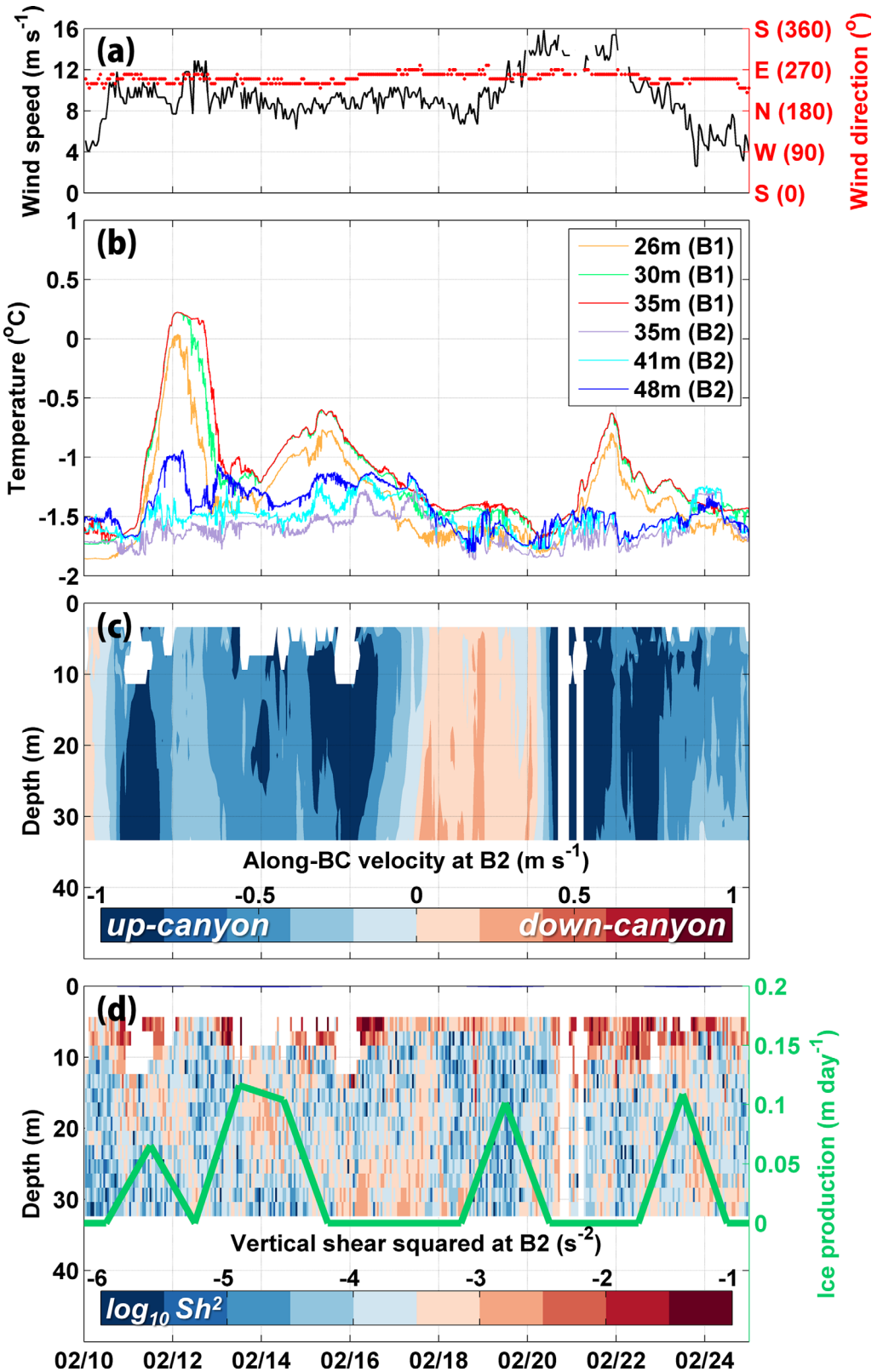

Figure 6. Same as Figure 5, but for the BCP Event 3.

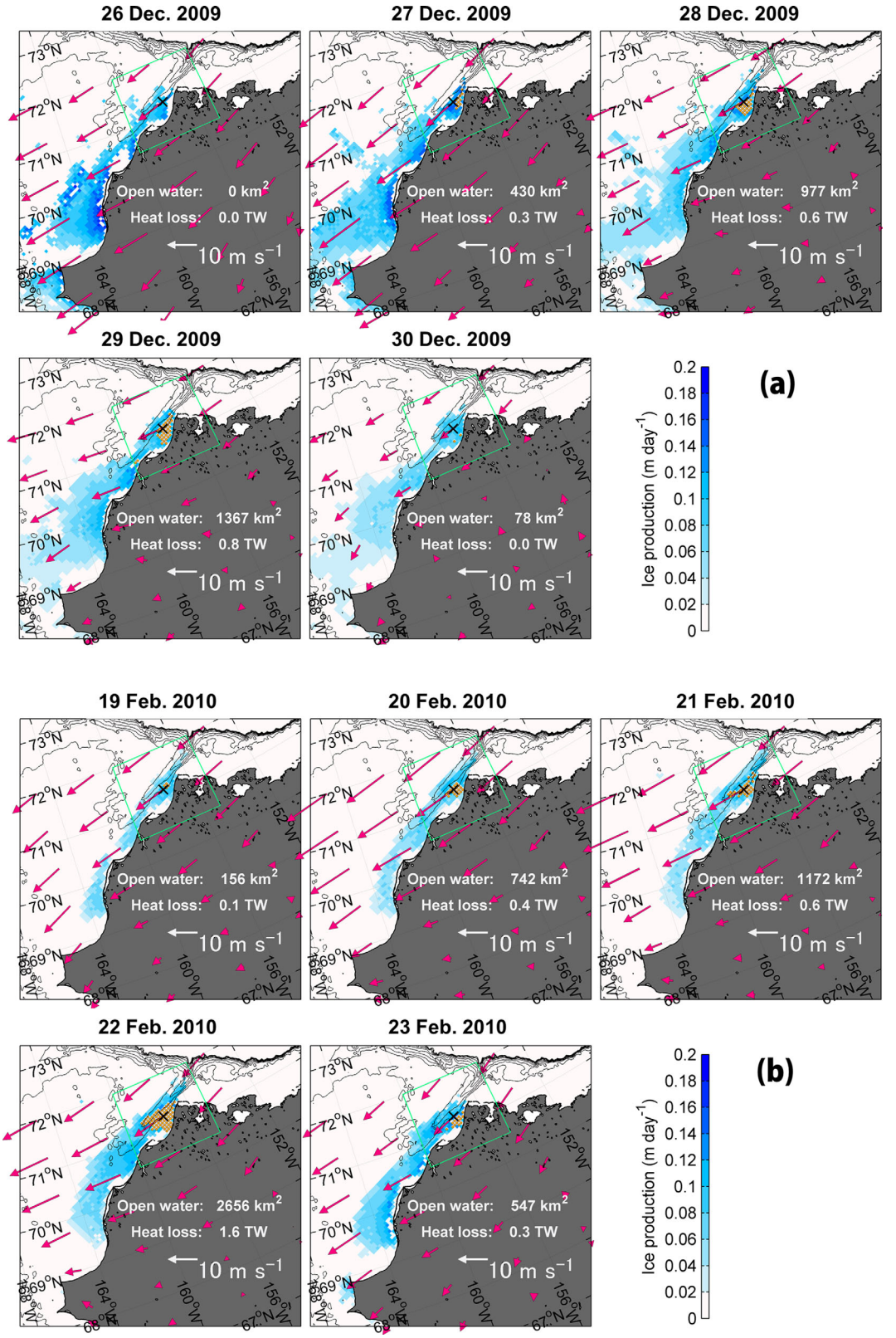

Figure 7. Spatial distributions of the sea ice production rate (shade) and 10 m wind from ERA-interim (vector) for (a) the BCP Event 1 (26–30 December 2009) and (b) the BCP Event 3 (19–23 February 2010). Orange dots represent the open water area based on the open water mask. Daily total open water areas and their heat loss in the BCP are indicated in each plot.

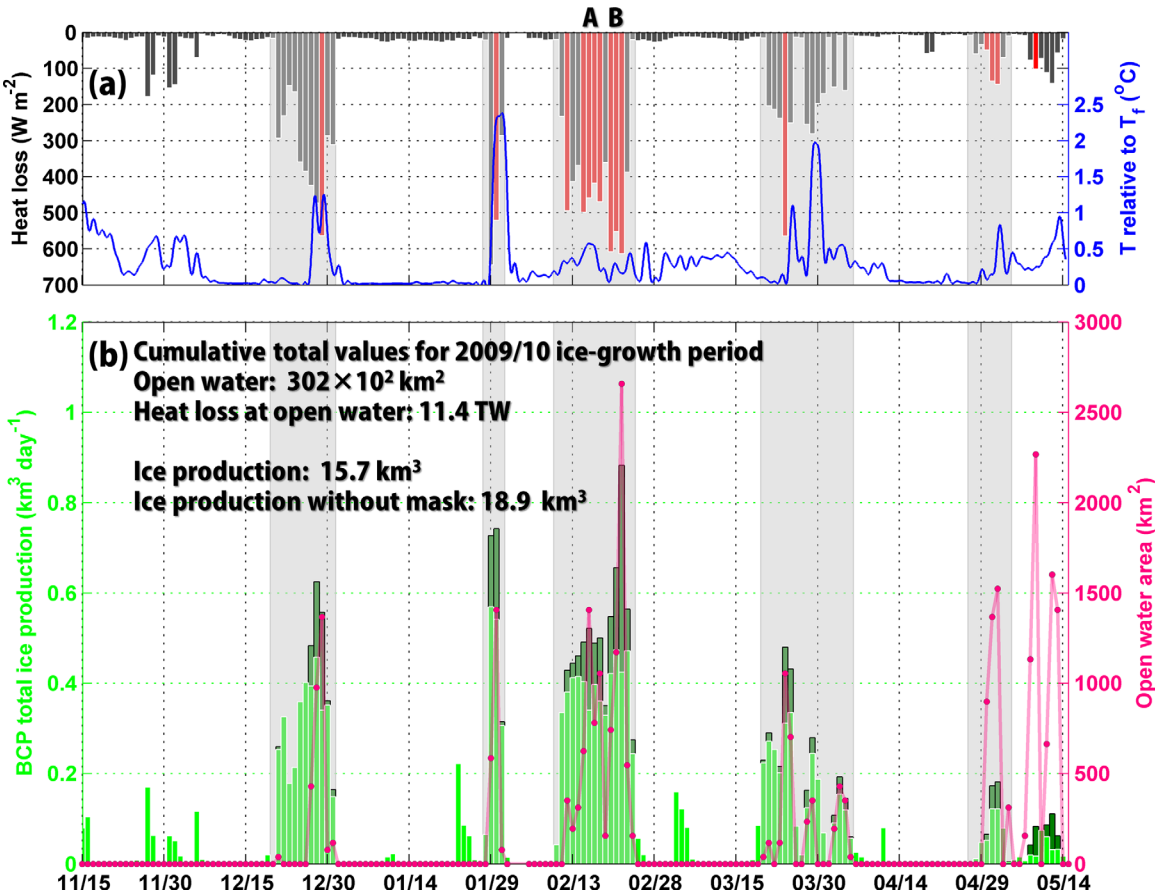

Figure 8. (a) Time series of the heat loss to atmosphere at the AMSR-E grid point shown in Figure 1b (bar) and temperature relative to freezing point at 41 m of B2 (solid line) from 15 November 2009 to 15 May 2010. Red bars indicate the date when open water is detected at the AMSR-E grid point by the open water mask. Labels "A" and "B" above the upper horizontal axis represent two open water periods judged by the open water mask. (b) Time series of the total volumes of ice production estimated with (light green) and without the open water mask (dark green) and the total area of open water (solid pink line) in the BCP. Shadings represent periods of BCP events.

values, values of K_T for periods A and B are estimated to be high at 6.4×10^{-3} and 2.0×10^{-2} m^2 s^{-1}, which indicate energetic vertical mixing. Note that these high K_T values are thought to be upper bounds, because we here consider the case that Q_{ocean} is only induced by turbulence. The assumption of the surface mixed layer temperature at the freezing point may not be realistic beneath a sensible heat polynya. Accordingly, for a surface mixed layer temperature of 0.1°C above the freezing point, values of K_T for periods A and B increase to 8.2×10^{-3} and 4.4×10^{-2} m^2 s^{-1}, respectively. Thus, it is reasonable to conclude that energetic vertical mixing was induced beneath this sensible heat polynya. As described above, the ocean heat flux during the BCP events cannot be neglected, and estimated values of K_T are much larger than those previously observed in the Arctic basin [e.g., *Rainville and Winsor*, 2008]. In addition, supercooling events accompanied by frazil ice formation were terminated by the advent of AW in the BCP [*Ito et al.*, 2015]. This observation can be also interpreted as a termination of frazil ice formation by ocean heat transport through energetic vertical mixing.

Next, we estimate the reduction of ice production by the ocean heat transport from below. Figure 8b shows time series of ice production in the BCP (defined as the green enclosed area in Figure 1b) estimated with (light green) and without (dark green) the open water mask. Here, the difference between the two estimates is considered to be roughly equivalent to the amount of suppressed ice production by ocean heat transport from below. The ocean heat transport had the largest impact on ice production for Event 3 when the open water area became vast (Figure 8b). Specifically, ice production was suppressed by almost half, compared to that without the open water mask, when the open water area was the largest on 22 February 2010. Throughout the ice-growth period in 2009/2010, ice production in the BCP is estimated to decrease by ~17% due to ocean heat transport from the upwelled warm water. However, note that this estimation

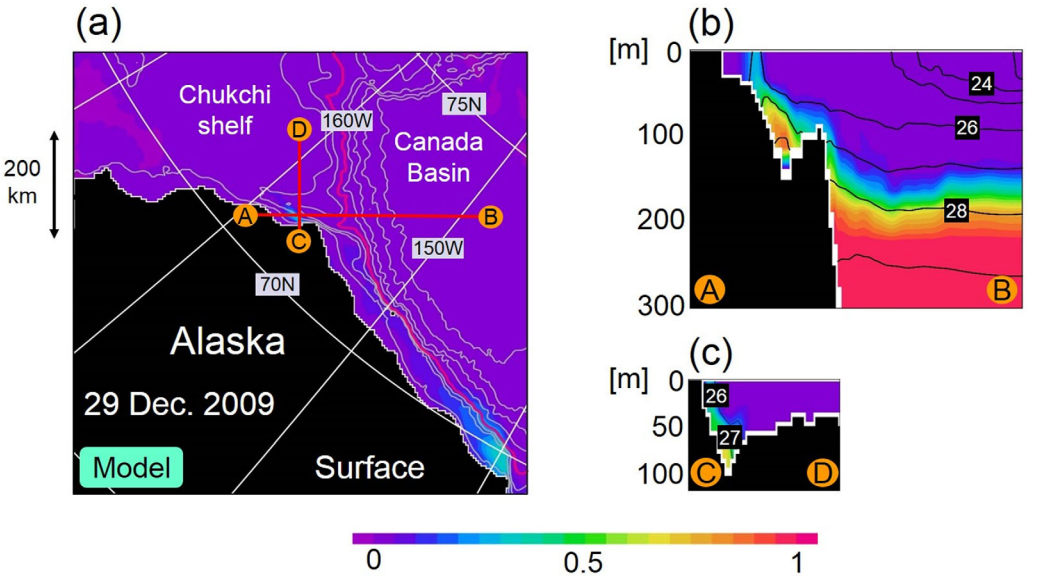

Figure 9. Spatial distribution of virtual tracer released below 200 m depth in the whole model domain on 29 December 2009 (Event 1). (a) Tracer concentration at the sea surface. White contours show sea bottom depths of 30, 60, 100, 200, 500, 2000, and 3000 m, and red contour represents 200 m isobath. (b, c) vertical sections of the tracer concentration (shade) and potential density (contour) across the nearest model grid point to B2.

depends on the accuracy of the open water mask itself. According to *Iwamoto et al.* [2013], most of the AMSR-E pixels along the ice edge have PR_{89} values between 0.09 and 0.13 (PR_{89} is the polarization ratio (PR) of AMSR-E 89 GHz brightness temperatures), and an average value of $PR_{89} = 0.11$ was adopted as a threshold to distinguish open water pixels from those of sea ice in their study. Therefore, we conducted a sensitivity test on the open water mask, in which the threshold values of PR_{89} were changed to 0.09 and 0.13. The result shows that the percentages of the suppressed ice production are ~36 and ~8.5% for the case of $PR_{89} = 0.09$ and 0.13, respectively. From this sensitivity test, we could argue that 10–30% of the BCP ice production was suppressed due to the ocean heat transport, even when allowing for the ambiguity in the open water mask threshold. Another point to note is that Figure 8b also demonstrates that polynya events end up with ice formation, because reduced northeasterly wind forcing (Figure 3a) weakens upwelling and subsequent intensive heat loss cools the upwelled water down to the freezing point.

4.2. Modeled Upwelling Event in the BCP

So far, we have discussed impacts of ocean heat transport from the upwelled warm water on ice production in the BCP based on observations. Although it is important to obtain the surface mixed layer temperature to quantify the impacts of the ocean heat transport on ice production, mooring observations in the sea ice area have significant limitations as mentioned above. Here, we verify our observational findings using the pan-Arctic ice-ocean model that reasonably reproduces major features of ocean circulation in the Chukchi Sea [*Watanabe*, 2011] described in section 2.3.

First, a tracer experiment was performed to visualize the upwelling process of warm water distributed in the mid-layer of the Canada Basin. During the integration period from October 2009 to March 2010, virtual tracers with values of 1 were continuously released below 200 m depth in the whole model domain. In order to examine how the basin water below 200 m depth is transported during the upwelling events, advection and diffusion processes of the virtual tracers are solved as well as temperature and salinity. During Events 1 (late December 2009) and 3 (late February 2010), high tracer concentrations appeared at the sea surface near Barrow Canyon (Figures 9a and 10a). Vertical sections of the tracer concentration across B2 near Barrow Canyon (Figures 9b, 9c, 10b, and 10c) demonstrate that high tracer concentrations originating from the Canada Basin were not widely spread across the Chukchi shelf but localized along the Alaska coast. The upwelling was stronger during Event 3 than during Event 1. In addition, high tracer concentrations at the surface were located along the coast of Barrow and spread toward the central Chukchi shelf after reaching the head of Barrow Canyon. A time series of the tracer concentration at the grid point closest to B2

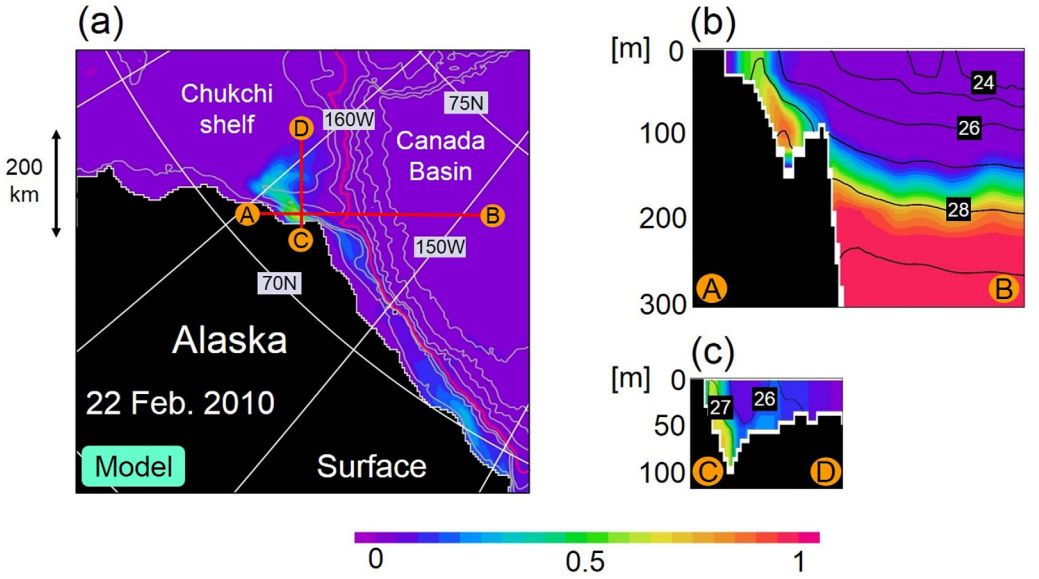

Figure 10. Same as Figure 10, but on 22 February 2010 (Event 3).

shows that high tracer concentrations during Event 3 continued for 1–2 weeks and the fraction reaching the sea surface was also high (Figure 11b). Tracer concentrations below 40 m from 22 to 27 February were above 0.5, which indicates that at least half of this water originated from the Canada Basin. The open water area on 22 February was largest and also extended along the coast southeast of Barrow Canyon (Figure 7, orange dots). The area of the high tracer concentration at the ocean surface corresponds well with that identified as the open water area by the open water mask. Impact from the ocean heat transport, associated with upwelled warm water, on ice production extends from the region off Barrow toward the southwest by ~150 km.

The tracer experiment demonstrates that water below 200 m in the Canada Basin was upwelled into the upper layer around Barrow Canyon and some reached the sea surface. Using this model result, we also discuss the transition process from a latent heat polynya to a sensible heat polynya associated with the transport of Canada Basin water. In this model experiment, warm and saline AW is distributed below 200 m in the Canada Basin, and upwelling of this water results in warm water transport into the shelf region. Time series of vertical sections of the potential temperature and salinity in Barrow Canyon (Figures 11c and 11d) show that the warm (> -1°C) and saline water was found from the sea floor to 40 m below the surface in both Events 1 and 3. (Note that the model grid point closest to B2 is deeper than the actual depth because the model bathymetry is interpolated, see caption in Figure 11.) Rising water temperatures in the BCP are caused by the transport of warm water from the Canada Basin in the absence of other heat sources from the sea surface or shelf region toward Bering Strait during these periods. The model result indicates that sea ice was produced at a rate of 0–0.1 m d^{-1} (Figure 11a), when the whole water column was maintained at the freezing point with deep vertical convection due to densification of the surface water (e.g., in mid-December, Figure 11e). On the other hand, sea ice melted during the upwelling events (Figure 11a), when the vertical convection was confined to the upper layer because ice production was suppressed or stopped due to the oceanic heat (e.g., late February in Figure 11e). As for vertical convection occurring in the deeper layer, it sometimes resulted from density instabilities caused by lateral intrusion of denser water upwelled in the surrounding regions. Because the heat budget at the surface of sea ice was largely negative (i.e., upward heat flux from sea ice to atmosphere), it can be assumed that the sea ice was melted by an episodic temperature rise in the surface layer just below the ice cover. Although it is not possible to estimate the amount of sea ice melt from the satellite-based algorithm by *Iwamoto et al.* [2014], the timing of sea ice melt in the model results is consistent with that identified as the open water area by this algorithm. The modeling results confirm the transition process from a latent to a sensible heat polynya revealed by the observations. Further, the upwelling events occurred in the region off Barrow Canyon and an extensive area

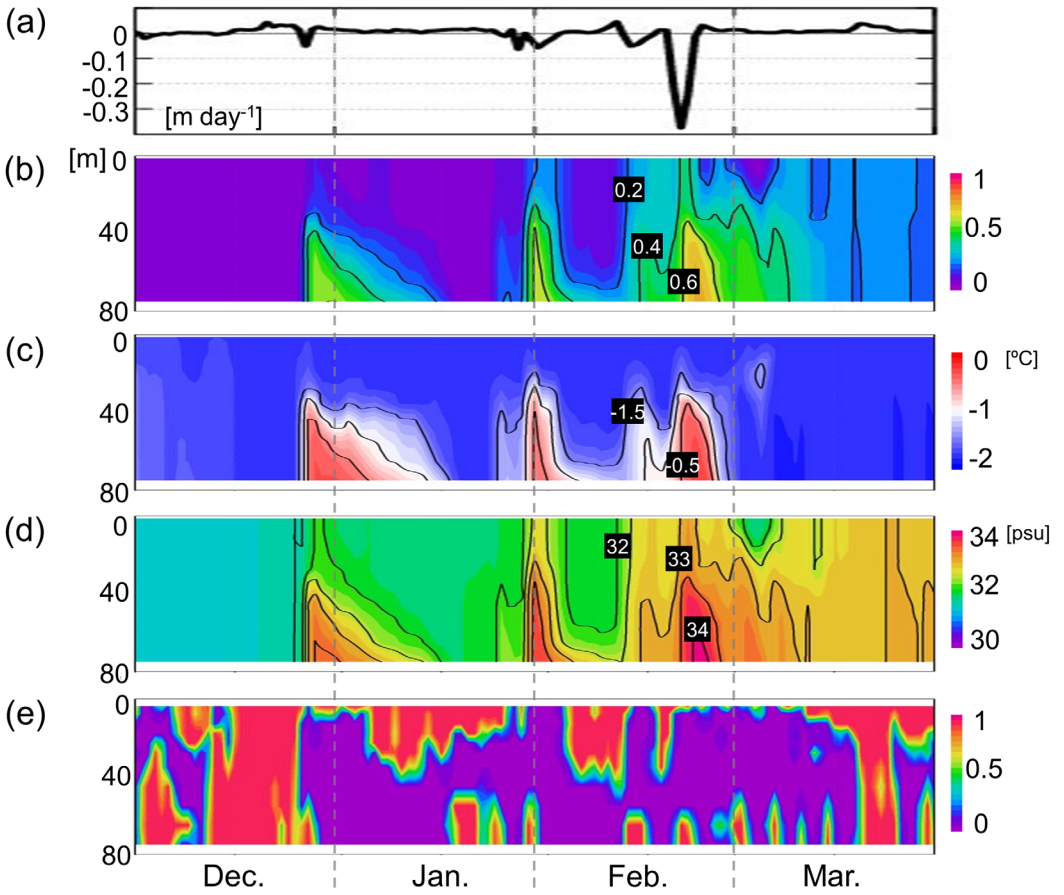

Figure 11. Time series of daily averaged values from December 2009 to March 2010 at the nearest model grid point to B2. (a) net ice production (production minus melt), (b) virtual tracer concentration, (c) potential temperature, (d) salinity, and (e) frequency of convective adjustment. In Figure 11e, a value of 1 (0.5) means that vertical convection occurs all the day (half a day). Note that water depth of this model grid point is 80 m, larger than that of B2, because the model bathymetry is interpolated onto a 5 km grid (i.e., the model bathymetry is different from the actual bathymetry, especially in the region of steep slope such as Barrow Canyon).

of the Beaufort shelf along the northern Alaska coast (Figures 9a and 10a), as caused by the northeasterly winds associated with the Aleutian Low and the Beaufort High [*Pickart et al*., 2009]. On the Beaufort Sea shelf, however, polynya occurrence along the east-west oriented coast is rare because sea ice is not necessarily driven offshore by northeasterly winds.

5. Concluding Remarks

Our findings on the transition in the BCP system from a latent to a sensible heat polynya are summarized in Figure 12. The latent/sensible heat polynya transition is driven by warm water upwelling in a causal chain that comprises: (1) dominant northeasterly winds (parallel to Barrow Canyon with an offshore component off Barrow), associated with the SLP pattern dominated by the Aleutian Low and the Beaufort High, result in warm water upwelling into the BCP region as well as the opening of the BCP by sea ice divergence, (2) baroclinic structure, established after the upwelling, gradually enhances the up-canyon shear flow, (3) enhanced vertical shear promotes vertical mixing accompanied by upward ocean heat flux from the upwelled warm water, (4) the ocean heat transport to the surface mixed layer results in the transition to a sensible heat polynya and finally suppresses ice production in the BCP, and (5) polynya events end up with ice formation. We propose that the BCP is a hybrid latent and sensible heat polynya, with both features caused by the same robust local northeasterly wind. Further, this study provides some evidence to support the validity of the open water mask developed by *Iwamoto et al*. [2013].

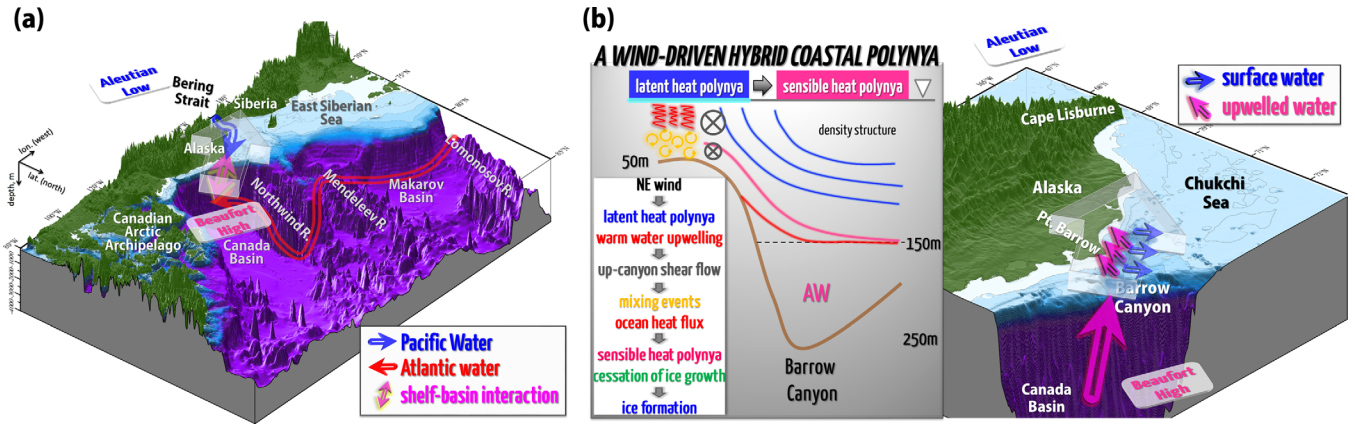

Figure 12. Schematics of "wind-driven hybrid latent and sensible heat polynya system" off Barrow, based on our findings. (a) Broad and (b) detailed views for the BCP system.

Identification of the sea ice growth and heat flux processes in the hybrid BCP leads to a proper understanding of a ventilation process of the CHL and deep layer as well as upper ocean circulation in the Canada Basin. Further, BCP events are considered to be one of the key processes to foster horizontal and vertical transfer of ocean heat contained in warm water masses, mainly AW. In the Canada Basin, the ocean heat flux from the near surface temperature maximum, found immediately below the surface mixed layer, partly contributes to sea ice melt [*Jackson et al.*, 2010]. On the other hand, the ocean heat flux from AW to the surface mixed layer is considered to have a minor impact in the Canada Basin because the CHL exists between the surface mixed layer and AW. In contrast, we have shown that the wind-driven upwelling of AW into the Chukchi shelf region suppresses ice production when the BCP becomes a sensible heat polynya. This suggests that AW significantly influences sea ice processes even in the Pacific sector. *Aagaard et al.* [1981] proposed a possible mechanism where cooling of AW on the shelves could produce source water of upper CHL. Actually, rapid salinity decreases after the upwelling events (Figures 3c and 11d) suggest that horizontal advection by the Alaskan Coastal Current immediately brings cold, fresh PWW into the BCP. Thus, the upwelled AW has a quite short residence time and this event is unlikely to precondition for deep water formation in the BCP. This study provides the following concept for ice production and accompanying dense shelf water formation in the BCP, such that (1) in a latent heat polynya prior to the upwelling, cold and dense water masses are formed by mixing PWW with cold and high-salinity brine associated with enhanced ice production, and (2) in a sensible heat polynya after the upwelling, relatively warm and dense water masses are formed by mixing PWW with warm and saline AW (in other words, "modified" AW is formed). In this way, different types of dense shelf water masses can be formed in this hybrid BCP. Note that the density of shelf water produced depends on mixing ratios of PWW and brine water or AW as well as their salinities. In any case, the dense shelf water formed in the BCP is dense enough to ventilate layers above and below the CHL in the Canada Basin. Therefore, consideration of water masses relevant in maintaining the CHL needs to include modified AW in addition to PWW. Since these water masses would lie over one another, they result in complicated stratification and upper ocean circulation in the Canada Basin. The transport of AW and its heat release process in the BCP, mainly during upwelling events, need to be considered to improve understanding of the heat budget and its dependence on atmosphere-ice-ocean interaction in the Pacific Arctic.

Further studies of the interannual variability of ice production and dense shelf water formation in the BCP and their relation to ocean heat transfer from AW are needed. Such work is relevant also to assessment of the interannual variability in CHL properties and upper ocean circulation in the Canada Basin, which need to be examined quantitatively. The proposed hybrid BCP system, showing AW influences on ice production even in the Pacific Arctic, is of great interest to the study on the ocean heat transfer and sea ice variability in the Pacific Arctic sector.

Acknowledgments

We thank UIC Science and CH2MHill Polar Services for planning and field support in Barrow and the North Slope Borough Department of Wildlife Management for use of their boat and assistance from their staff. The AMSR-E data were provided by the National Snow and Ice Data Center (NSIDC), University of Colorado. The ERA-Interim data were obtained from the ECMWF Research Data Server (http://data.ecmwf.int/data/). Modeling experiments were executed using Earth Simulator of Japan Agency for Marine-Earth Science and Technology (JAMSTEC). We are also grateful to Hiroyasu Hasumi, Kohei Mizobata, Motoyo Itoh, Yusuke Kawaguchi, Shigeto Nishino, and Takashi Kikuchi for their useful comments. This work was supported by Grants-in-Aids for Scientific Research (20221001, 23654163, 24810030, 26740007, and 26800248), the Green Network of Excellence (GRENE) Arctic Climate Change Research Project of the Ministry of Education, Culture, Sports, Science and Technology, and the Joint Research Program of the Institute of Low Temperature Science, Hokkaido University in Japan, and by the National Science Foundation Seasonal Ice Zone Observing Network award OPP-0856867. Valuable comments from two anonymous reviewers are greatly appreciated.

References

Aagaard, K., and A. T. Roach (1990), Arctic ocean-shelf exchange: Measurements in Barrow Canyon, *J. Geophys. Res.*, *95*(C10), 18,163–18,175, doi:10.1029/JC095iC10p18163.

Aagaard, K., L. K. Coachman, and E. Carmack (1981), On the halocline of the Arctic Ocean, *Deep Sea Res., Part A*, *28*(6), 529–545.

Barber, D. G., J. M. Hanesiak, W. Chan, and J. Piwowar (2001), Sea-ice and meteorological conditions in Northern Baffin Bay and the North Water polynya between 1979 and 1996, *Atmos. Ocean*, *39*, 343–359.

Bitz, C. M., and W. H. Lipscomb (1999), An energy-conserving thermodynamic model of sea ice, *J. Geophys. Res.*, *104*(C7), 15,669–15,677, doi:10.1029/1999JC900100.

Bitz, C. M., M. M. Holland, A. J. Weaver, and M. Eby (2001), Simulating the ice thickness distribution in a coupled climate model, *J. Geophys. Res.*, *106*(C2), 2441–2463, doi:10.1029/1999JC000113.

Cavalieri, D. J., and S. Martin (1994), The contribution of Alaskan, Siberian, and Canadian coastal polynyas to the cold halocline layer of the Arctic-Ocean, *J. Geophys. Res.*, *99*(C9), 18,343–18,362, doi:10.1029/94JC01169.

Cavalieri, D. J., T. Markus, and J. Comiso (2004), *AMSR-E/Aqua Daily L3 12.5 km Brightness Temperature, Sea Ice Concentration, and Snow Depth Polar Grids*, version 2, Natl. Snow and Ice Data Cent., Boulder, Colo. [Available at http://nsidc.org.data/ae_si12.html.] [Updated daily].

Comiso, J. C. (1995), *SSM/I Sea Ice Concentrations Using the Bootstrap Algorithm*, vol. 1380, 49 pp., Natl. Aeronaut. and Space Admin., Goddard Space Flight Cent., Greenbelt, Md.

Eicken, H., R. Gradinger, T. Heinrichs, M. Johnson, A. Lovecraft, Fukamachi, Y., K. I. Ohshima, D. Simizu, T. Takatsuka, K. Iwamoto, and M. Kaufman (2014), *Mooring Temperature/Conductivity & Temperature/Pressure data (SIZONET)*, UCAR/NCAR-CISL-ACADIS. [Available at http://dx.doi.org/10.5065/D6BG2KW9.]

Fer, I. (2009), Weak vertical diffusion allows maintenance of cold halocline in the central Arctic, *Atmos. Oceanic Sci. Lett.*, *2*(3), 148–152.

Fukamachi, Y., K. Ohshima, D. Simizu, T. Takatsuka, K. Iwamoto, A. Mahoney, J. Jones, H. Eicken (2014), *Mooring ADCP data (SIZONET)*, UCAR/NCAR-CISL-ACADIS. [Available at http://dx.doi.org/10.5065/D6G44N6Q.]

Griffies, S. M., and R. W. Hallberg (2000), Biharmonic friction with a Smagorinsky-like viscosity for use in large-scale eddy permitting ocean models, *Mon. Weather Rev.*, *128*, 2935–2946.

Hasumi, H. (2006), CCSR Ocean Component Model (COCO) version 4.0, *Center for Climate System Research Report*, *25*, 103 pp., Univ. of Tokyo.

Hunke, E. C., and J. K. Dukowicz (1997), An elastic-viscous-plastic model for sea ice dynamics, *J. Phys. Oceanogr.*, *27*(9), 1849–1867.

Ingram, R. G., J. Bâcle, D. G. Barber, Y. Gratton, and H. Melling (2002), An overview of physical processes in the North Water, *Deep Sea Res., Part II*, *49*, 4893–4906.

Ito, M., K. I. Ohshima, Y. Fukamachi, D. Simizu, K. Iwamoto, Y. Matsumura, A. R. Mahoney, and H. Eicken (2015), Observations of supercooled water and frazil ice formation in an Arctic coastal polynya from moorings and satellite imagery, *Ann. Glaciol.*, *56*(69), 307–314, doi: 10.3189/2015AoG69A839.

Itoh, M., K. Shimada, T. Kamoshida, F. McLaughlin, E. Carmack, and S. Nishino (2012), Interannual variability of Pacific Winter Water inflow through Barrow Canyon from 2000 to 2006, *J. Oceanogr.*, *68*(4), 575–592, doi:10.1007/s10872-012-0120-1.

Itoh, M., S. Nishino, Y. Kawaguchi, and T. Kikuchi (2013), Barrow Canyon volume, heat, and freshwater fluxes revealed by long-term mooring observations between 2000 and 2008, *J. Geophys. Res. Oceans*, *118*, 4363–4379, doi:10.1002/jgrc.20290.

Iwamoto, K., K. I. Ohshima, T. Tamura, and S. Nihashi (2013), Estimation of thin ice thickness from AMSR-E data in the Chukchi Sea, *Int. J. Remote Sens.*, *34*(2), 468–489.

Iwamoto, K., K. I. Ohshima, and T. Tamura (2014), Improved mapping of sea ice production in the Arctic Ocean using AMSR-E thin ice thickness algorithm, *J. Geophys. Res. Oceans*, *119*, 3574–3594, doi:10.1002/2013JC009749.

Jackson, J. M., E. C. Carmack, F. A. McLaughlin, S. E. Allen, and R. G. Ingram (2010), Identification, characterization, and change of the near-surface temperature maximum in the Canada Basin, 1993-2008, *J. Geophys. Res.*, *115*, C05021, doi:10.1029/2009JC005265.

Kawaguchi, Y., T. Tamura, S. Nishino, T. Kikuchi, M. Itoh, and H. Mitsudera (2011), Numerical study of winter water formation in the Chukchi Sea: Roles and impacts of coastal polynyas, *J. Geophys. Res.*, *116*, C07025, doi:10.1029/2010JC006606.

Leonard, B. P., M. K. MacVean, and A. P. Lock (1994), The flux-integral method for multi-dimensional convection and diffusion, *NASA Tech. Memo*., 106679/ICOMP-94-13, NASA, Washington, D. C.

Mahoney, A. R., H. Eicken, A. G. Gaylord, R. Gens (2014) Landfast sea ice extent in the Chukchi and Beaufort Seas: The annual cycle and decadal variability, *Cold Reg. Sci. Technol.*, *103*, 41–53.

Mahoney, A. R., H. Eicken, Y. Fukamachi, K. I. Ohshima, D. Simizu, C. Kambhamettu, Rohith, M.V., S. Hendricks, and J. Jones (2015), Taking a look at both sides of the ice: Comparison of ice thickness and velocity from moored, airborne and shore-based instruments near Barrow, Alaska, *Ann. Glaciol.*, *56*(69), 363–372, doi:10.3189/2015AoG69A565.

Martin, S., R. Drucker, R. Kwok, and B. Holt (2004), Estimation of the thin ice thickness and heat flux for the Chukchi Sea Alaskan coast polynya from Special Sensor Microwave/Imager data, 1990-2001, *J. Geophys. Res.*, *109*, C10012, doi:10.1029/2004JC002428.

Maykut, G. A. (1978), Energy exchange over young sea ice in central Arctic, *J. Geophys. Res.*, *83*(C7), 3646–3658, doi:10.1029/JC083iC07p03646.

Melling, H., Y. Gratton, and G. Ingram (2001), Ocean circulation within the North Water polynya of Baffin Bay, *Atmos. Ocean*, *39*, 301–325.

Morales Maqueda, M. A., A. J. Willmott, and N. R. T. Biggs (2004), Polynya Dynamics: a review of observations and modeling, *Rev. Geophys.*, *42*, RG1004, doi:10.1029/2002RG000116

Mundy, C. J., and D. G. Barber (2001), On the relationship between spatial patterns of sea-ice type and the mechanisms which create and maintain the North Water (NOW) polynya, *Atmos. Ocean*, *39*, 327–341.

Noh, Y., and H. J. Kim (1999), Simulations of temperature and turbulence structure of the oceanic boundary layer with the improved near-surface process, *J. Geophys. Res.*, *104*(C7), 15,621–15,634, doi:10.1029/1999JC900068.

Petrich, C., H. Eicken, J. Zhang, J. Krieger, Y. Fukamachi, and K. I. Ohshima (2012), Coastal landfast sea ice decay and breakup in northern Alaska: Key processes and seasonal prediction, *J. Geophys. Res.*, *117*, C02003, doi:10.1029/2011JC007339.

Pickart, R. S., T. J. Weingartner, L. J. Pratt, S. Zimmermann, and D. J. Torres (2005), Flow of winter-transformed Pacific water into the Western Arctic, *Deep Sea Res., Part II*, *52*, 3175–3198.

Pickart, R.S., G.W.K. Moore, D.J. Torres, P.S. Fratantoni, R.A. Goldsmith, J. Yang (2009), Upwelling on the continental slope of the Alaskan Beaufort Sea: Storms, ice, and oceanographic response, *J. Geophys. Res.*, *114*, C00A13, doi:10.1029/2208JC005009.

Rainville, L., and P. Winsor (2008), Mixing across the Arctic ocean: Microstructure observations during the Beringia 2005 expedition, *Geophys. Res. Lett.*, *35*, L08606, doi:10.1029/2008GL033532.

Rainville, L., and R. A. Woodgate (2009), Observations of internal wave generation in the seasonally ice-free Arctic, *Geophys. Res. Lett.*, *36*, L23604, doi:10.1029/2009GL041291.

Roach, A. T., K. Aagaard, C. H. Pease, S. A. Salo, T. Weingartner, V. Pavlov, and M. Kulakov (1995), Direct measurements of transport and water properties through the Bering Strait, *J. Geophys. Res.*, *100*(C9), 18,443–18,457, doi:10.1029/95JC01673.

Rudels, B., L. G. Anderson, and E. P. Jones (1996), Formation and evolution of the surface mixed layer and halocline of the Arctic Ocean, *J. Geophys. Res.*, *101*(C4), 8807–8821, doi:10.1029/96JC00143.

Saha, S., et al. (2010), The NCEP Climate Forecast System Reanalysis, *Bull. Am. Meteorol. Soc.*, *91*, 1015–1057, doi:10.1175/2010BAMS3001.1.

Tamura, T., and K. I. Ohshima (2011), Mapping of sea ice production in the Arctic coastal polynyas, *J. Geophys. Res.*, *116*, C07030, doi:10.1029/2010JC006586.

Thompson, R. O. R. Y. (1983), Low-pass filters to suppress inertial and tidal frequencies, *J. Phys. Oceanogr.*, *13*(6), 1077–1083.

Watanabe, E. (2011), Beaufort shelf break eddies and shelf-basin exchange of Pacific summer water in the western Arctic Ocean detected by satellite and mooring analyses, *J. Geophys. Res.*, *116*, C08034, doi:10.1029/2010JC006259.

Watanabe, E. (2013), Linkages among halocline variability, shelf-basin interaction, and wind regimes in the Beaufort Sea demonstrated in pan-Arctic Ocean modeling framework, *Ocean Modell.*, *71*, 43–53, doi:10.1016/j.ocemod.2012.12.010.

Watanabe, E., et al. (2014), Enhanced role of eddies in the Arctic marine biological pump, *Nat. Commun.*, *5*, 39–50, doi:10.1038/ncomms4950.

Watanabe, E., J. Onodera, N. Harada, M. N. Aita, A. Ishida, and M. J. Kishi (2015), Wind-driven interannual variability of sea ice algal production in the western Arctic Chukchi Borderland, *Biogeosciences*, *12*, 6147–6168, doi:10.5194/bg-12-6147-2015.

Weingartner, T. J., D. J. Cavalieri, K. Aagaard, and Y. Sasaki (1998), Circulation, dense water formation, and outflow on the northeast Chukchi shelf, *J. Geophys. Res.*, *103*(C4), 7647–7661, doi:10.1029/98JC00374.

Weingartner, T. J., K. Aagaard, R. A. Woodgate, S. Danielson, Y. Sasaki, and D. J. Cavalieri (2005), Circulation on the north central Chukchi Sea shelf, *Deep Sea Res., Part II*, *52*, 3150–3174.

Winsor, P., and G. Björk (2000), Polynya activity in the Arctic Ocean from 1958 to 1997, *J. Geophys. Res.*, *105*(C4), 8789–8803, doi:10.1029/1999JC900305.

Woodgate, R. A., K. Aagaard, and T. J. Weingartner (2005), A year in the physical oceanography of the Chukchi Sea: Moored measurements from autumn 1990-1991, *Deep Sea Res., Part II*, *52*, 3116–3149.

Woodgate, R. A., K. Aagaard, and T. J. Weingartner (2006), Interannual changes in the Bering Strait fluxes of volume, heat and freshwater between 1991 and 2004, *Geophys. Res. Lett.*, *33*, L15609, doi:10.1029/2006GL026931.